Actin turnover and myosin contractility determine emergent Thickness Robustness of Cell-Mimicking Cortex

Authors: Gat. S[1], Amit. Y[1], Livne. G[1], Daniel Sevilla Sanchez[2], Porat. N[2], Yochelis. A[3], Gov. N.S[4], Bernheim-Groswasser. A[1,2*]

Affiliations:

[1]Department of Chemical Engineering, [2]Ilse Kats Institute for Nanoscale Science and Technology, Ben Gurion University of the Negev; Beer-Sheva 84105, Israel.

[3]Department of Physics, Ben Gurion University of the Negev; Beer-Sheva 84105, Israel.

[4]Department of Chemical and Biological Physics, The Weizmann Institute of Science; Rehovot 76100, Israel.

*Corresponding author Email: bernheim@bgu.ac.il

Abstract: Cell shape deformation is primarily determined by the actin cortex, a thin network of actin filaments and myosin motors, that lies beneath and attached to the plasma membrane of cells and endows cells with their mechanical stability and structural integrity. Since inside the cells there are hundreds of proteins associated with the actin cortex, it is very difficult to identify the role of each component and the mechanisms that maintain a functional cortex. Here, using a minimal set of components we recreate dynamic treadmilling in an actomyosin cortex on a bilayer membrane with cell-mimicking characteristics, in the absence and presence of myosin-II molecular motors. We reveal how treadmilling is regulated by actin network disassembly factors and myosin contractility, and how this drives the robustness of the cortical thickness to concentration fluctuations in cytoskeletal components.

One-Sentence Summary: Recreating the cellular skeleton network that determines cell shape and integrity using a minimal set of cellular building-blocks.

Main Text:

Introduction

Eukaryotic cells actively change their shapes during a variety of cellular processes. Cell shape deformation is primarily determined by the actin cortex, a thin network of branched and unbranched actin filaments and myosin motors, that lies beneath and attached to the plasma membrane of cells (1). Despite being very thin ($\leq 1\mu m$) and continuously turning over (2, 3), the cell cortex endows cells with its mechanical stability and structural integrity (4, 5). At the same time, its dynamic nature is essential for driving various cellular processes that involve cell shape changes such as cell division and motility (6-8), which are both essential during development, immune response and cancer progression.

Two key processes govern the dynamics of the cell cortex. The first relies on the treadmilling of the actin network, which is the process of continuous polymerization at the membrane bilayer and disassembly towards the cell interior. An additional dynamical process is driven by myosin II motors which exert contractile forces within the actin cortex. All these processes are active, out-of-equilibrium, driven by the continuous consumption of energy (ATP) (9, 10). Biological studies have mapped hundreds of molecular components that interact with this cortical network (2, 11), but it is still unknown what constitutes the minimal set of components that can initiate the formation and sustain the dynamics and structural integrity of the cell cortex. Finding such a minimal set of components will allow us to achieve a fundamental understanding of this crucial cellular structure, and therefore the ability to design interventions that modify the cellular cortex efficiently for various medical applications.

Motivated by Feyman's famous quote: "What I cannot make, I don't understand", there has been an ongoing effort to recreate the actin network under well-controlled settings using a very limited set of pure components (12, 13). This approach has been previously employed to reconstitute actin cortices in various geometries (14-18), but none of these previous works managed to reconstitute a membrane-bound treadmilling actin cortex, where the thickness is dynamically regulated, as in living cells (19-21).

Here, for the first time, we identify a minimal set of components that can recreate dynamic treadmilling in an actomyosin cortex on a bilayer membrane with cell-mimicking characteristics. We demonstrate the treadmilling dynamics inside these cortices, in the absence and presence of myosin-II molecular motors. We reveal how the treadmilling is regulated by actin network disassembly factors, and how this drives the robustness of the cortical thickness to concentration fluctuations in cytoskeletal components. We explain the emergence of the observed thickness robustness using a simple mathematical model. This ability of the system to efficiently buffer fluctuations in the concentration of its components through an actin turnover mechanism may be an important cellular property for maintaining proper function and responsiveness to environmental cues.

Significance

For the first time we show that, out of the hundreds of proteins involved in the cell cytoskeleton, there exist a minimal set of ingredients (12 components) that form a treadmilling actin (or actomyosin) cortex of cell-like characteristics on a bilayer membrane in cell-mimicking conditions. We discover an emergent robustness of the cortex thickness against concentration fluctuations, whereby the cortex thickness is very weakly affected by

fluctuations of the actin network disassembly rate. This indicates that the system can efficiently buffer fluctuations in the concentration of its components, maintaining its thickness globally unchanged. This property has a very fundamental biological significance allowing Eukaryotic cells to maintain a mechanical stability of their membrane and prevent cell rupture, despite concentration fluctuation of the cytoskeleton components. In addition, we find the conditions of steady-state cortex in the presence of myosin-II motors, which are observed to induce a significant increase in the actin polymerization rate and cortex thickness. A similar increase in cortical thickness was observed in cells due to myosin activity. Our results open the way to systematic studies of the actin cortex at a level of detail that is impossible in living cells, providing deeper understanding of this fundamental biological structure.

Results

We recreate an actin cortex assembling from the surface of a supported lipid bilayer (SLB) which dynamically turnovers for hours. Our experimental system consists of a flat PIP_2-based SLB-decorated flow chamber (Fig. 1A, main) and GTP-activated Cdc42 incorporated within it, nucleation promoting factors (NPF) (specifically, ΔEVH1 N-WASP, the near full-length version of N-WASP lacking only the N-terminal EVH1 domain (22), which localize to this SLB and physically link the actin cortex to it (Fig. 1A, 1). The system also includes a solution of a well-defined and controlled set of purified components which control the rate of actin assembly/disassembly and can also be supplemented with myosin-II motor filaments (Fig. 1A, 2). The purpose of using intrinsically inactive N-WASP instead of its intrinsically active VCA form (23) not only better represents the native biological system, but also ensures that actin network assembly is exclusively on the membrane surface (Fig. S1), where N-WASP is activated by binding to both PIP_2 and Cdc42 (24). In particular, the use of a flat geometry enables to quantitatively characterize the intrinsic dynamics of actin cortex growth and turnover, decoupled from curvature effects (25). The chamber volume to surface area and the employed concentrations have been purposely designed to mimic the restricted availability of components observed in cellular environments: In our chamber the ratio of available actin, the most abundant protein in most eukaryotic cells (26, 27), to membrane area (where actin network assembly takes place), is comparable to the value for typical cells (see SI).

Aiming to identify what constitutes a minimal set of pure components that allows for a treadmilling actin cortex of finite steady state thickness h_{ss} to form (Fig. 1A, main), we include actin monomers along with accessory proteins such as Profilin, Capping proteins (CPs), and Arp2/3 complex, to regulate the rates of actin cortex assembly. Their concentrations are kept constant in all studied systems. Network disassembly rate is regulated by a mixture of three components ($\mathrm{Cor1B\,(C)}$, $\mathrm{AIP1}(A)$, and $\mathrm{hCof\,(C)}$), which facilitate the disassembly, debranching and severing of ADP-bound actin filaments (F-actin) (Figs. 1A) (28-31). We maintain a constant concentration of hCof, and modulate the disassembly rates by adjusting the concentrations of $\mathrm{Cor1B}$ (C) and $\mathrm{AIP1}(A)$ between $0-75$ nM, keeping a $1{:}\,1$ molar ratio $(C{:}\,A)$ (29). Additionally, in some of the experiments we added $50\mathrm{nM}$ myosin II motors in the form of small filaments (or aggregates) of controlled size (32, 33), roughly consisting of 50 myosin dimers, similar to their size in cells (34). All experiments are performed with 2mM ATP, maintained constant using an ATP regenerating system, which keeps actin and myosin-dependent activities steady for several hours (32, 35-37).

At time $t = 0$, we introduce the components into the chamber. This prompts the rapid ($\ll$ 1min) formation of a thin and tightly packed cortical layer on the SLB surface (Fig.1B). This thin initial cortical actin network forms with very similar thickness (denoted as h_0, see Fig. 1D) and density profile for all studied systems (Fig. 1B,C). The progression towards steady state involves a transient, nonlinear 'growth' phase during which the network thickens over time (Fig. 1B-D) while its density decreases (Fig. 1B,C). Network thickness growth can be accompanied by large thickness fluctuations (Fig. 1B), which may indicate that non-uniform stresses develop in the network. The gradual density decrease occurs throughout the thickness and is most clearly visible at the cortex's outer edge, where the network is oldest (see density profile variations in Fig. 1C). It mirrors the progressive disassembly of the actin network with time, clearly more efficient in the presence of CA (Fig. 1C, right panel at times $1 - 25$min). This process replenishes the system with components (such as actin monomers, Arp2/3 etc.) that diffuse to and repolymerize at the SLB surface, promoting the fresh formation of an actin network (see the density profile variations in Fig. 1C right panel). The actin growth at the SLB pushes the preformed network upwards, leading to the observed thickening effect. This transient growth regime culminates in a rapid thickness reduction following network disassembly (Fig.1B-D, Movie S1). Note that systems lacking CA remain in the 'growth' phase over the few hours timescale of the experiment (Fig. 1B-D depicts the first two hours out of six, Movie S2), highlighting the pivotal role of network disassembly in achieving a dynamic steady-state.

After this transient stage, and only in the presence of CA (with or without myosin II), the system stabilizes at its steady state thickness, h_{ss}, which remains stable for hours (Figs. 1B-D, and S2, depict the first two hours out of five). These systems exhibit a characteristic asymmetric actin density distribution across their thickness, similar for all studied systems (Figs. 1C and S2), with the peak density spatially shifted relative to that of the membrane (localized at $z = 0$) and decaying exponentially away from the surface (as depicted in Figs. 1C,E, and S2), mirroring observations in living cells (19, 38).

While all systems containing a finite amount of CA reach such long-lasting (i.e., hours) treadmilling steady-states, the transition time $t_{g\to ss}$ from growth to steady state regime gets shorter with the increase in $[CA]$ due to faster disassembly rates, reducing to mere minutes at elevated CA levels (Fig. S3). Intriguingly, the presence of myosin II delays the arrival to steady state compared to systems lacking motors (Figs. 1B and S3), possibly due to competition with disassembly factors for F-actin binding or due to internally applied active stresses generated by myosin that may slowdown the network disassembly during the transient phase before the onset of the steady-state turnover.

We turn now to characterizing the steady state regime. We find that it is characterized by a continuous upward actin flux starting from the SLB surface (Fig.1F and Movie S3). The actin turnover velocity, v_{turn}, is extracted from the slopes of Kymograph plots (Fig. 1F). These trajectories are straight, suggesting that the actin flux remains uniform across the thickness – a clear sign that the system is in a dynamic steady state. Over the entire course of the experiment new trajectories consistently emerge, all displaying similar linear slopes, indicating that both the actin fluxes and the turnover velocity are long-lasting and stable over time (Fig. 1G). The steady-state turnover velocity is stable both in the presence and absence of molecular motors, but it is significantly higher when myosin-II is present.

We next investigate the dependence of the turnover velocity, cortex thickness, and network disassembly rate on CA concentration. In Fig. 2A we plot the dependence of v_{turn} on CA concentration, observing a clear monotonous increase up to saturation, reminiscent of first-

order kinetics. Similarly, we plot the network disassembly rate τ^{-1} in Fig. 2B. This quantity is only accessible during the transient 'growth' phase, when we can evaluate it from the measured decay of the fluorescence of the F-actin density at the cortex's outer edge over time (Figs.1C, S4, and SI appendix). We find that this density decays exponentially over time, indicating a roughly constant disassembly rate. Both observations can be explained using a simple one-dimensional model for the dynamics of the actin cortex (Fig. 2D, see also SI), which focuses on the dynamics of the disassembly factors (39) while not including the myosin motors (40, 41). We give here a simplified analysis based on this model, where we neglect the spatial distribution of the cytoplasmic components (actin monomers and free depolymerization agents), to highlight the main steady-state features. This simplification is valid in the limit of fast diffusion of the soluble components, which seems to be the relevant regime in our case. We assume that actin network disassembly occurs by 1st order kinetics, so that the steady-state fraction of F-actin which is covered by bound depolymerization agents is given by:

$$n_{b,ss} = \frac{[CA]}{[CA]+k_{off}/k_{on}} \qquad [1]$$

where k_{on} and k_{off} are the on/off rates of the CA (actually, the complex of all the three disassembly factors together, CCA) from the F-actin, and we assume that these reactions are fast compared with network disassembly rate, τ^{-1}. The dynamics of the actin cortex density obeys the following advection-reaction equation (see SI for the full one-dimensional spatio-temporal model):

$$\frac{\partial \rho_{cortex}(z,t)}{\partial t} = -v_{turn}\nabla_z \rho_{cortex}(z,t) - \tau^{-1}\rho_{cortex}(z,t) \qquad [2]$$

Where ρ_{cortex} is the local density of the actin network at height z from the SLB, where the disassembly of F-actin to monomers occurs at a rate given by

$$\tau^{-1} = \alpha \frac{[CA]}{[CA]+k_{off}/k_{on}} \qquad [3]$$

and α is a rate constant which determines how fast the CCA-bound F-actin disassembles. In Fig. 2B (black dots) we fit the experimental data to Eq. 3, extracting the values of $k_m = k_{off}/k_{on} = 19.7 \pm 2.6$ nM and $\alpha = 0.13 \pm 0.01$.

We next wish to relate the disassembly rate with the rate of actin turnover as measured by v_{turn}. Since the supply of actin monomers at the SLB surface drives actin network polymerization, we expect this turnover speed to be proportional to the rate of F-actin disassembly. This assumption is plausible since diffusion of actin monomers across the cortex thickness occurs over much faster timescales (order of 1s, see SI appendix), and is therefore not the rate-limiting step. We can therefore write:

$$v_{turn} \propto n_{mono} \propto \tau^{-1} \; [4]$$

Where n_{mono} represents the concentration of actin monomers. This relation suggests that v_{turn} and τ^{-1} will have the same functional dependence on CA. Indeed, we can fit the experimental data in Fig. 2A to Eq.3 and obtain a value of $k_m = 19.6 \pm 5.5$nM which is very similar to that obtained from Fig. 2B.

From Eq.2 we find that the steady-state solution (i.e. when $\partial \rho_{cortex}(z,t)/\partial t = 0$) gives a cortex density that decays exponentially away from the SLB, with a thickness given by the ratio of: v_{turn}/τ^{-1}. From the discussion above, Eq. 4, we therefore expect this steady-state thickness to be independent of the CA concentration. In Fig. 2C we plot the measured cortex steady-state thickness and demonstrate that it is overall independent of the CA concentration, as this simple model predicts.

To compare quantitatively, we note that the τ^{-1} cannot be measured during the steady-state regime, only during the initial transient growth phase (Fig. S4). Nevertheless, we can estimate

it from the ratio v_{turn}/h_{ss} measured at steady-state. In Fig. 2B (blue dots) we see that this calculated ratio is ~2.5 times higher ($\alpha = 0.31 \pm 0.03$ with unchanged k_m) than the measured τ^{-1} during the growth phase, indicating that the disassembly rate at the transient regime is slower by this factor compared to the disassembly rate at the steady state. This difference can very well arise from the higher network density and rigidity of the thin initial cortical actin layer (which changes the value of the parameter α in Eq. 3), compared to the steady state cortex (Fig.1C right panel).

In Fig. 2E we plot the results of the 1D model for the actin cortex density profile. The model captures the fast initial formation of a thin polymerized layer, which then thickens during the growth phase (with a local high-density region that is pushed away while decaying in amplitude), and the final formation of a thinner steady-state profile (Movie S1). The steady-state density profile exhibits the exponential tail, as observed in experiments (Fig. S2). In Fig. 2F we show the model's predicted dependence of v_{turn} on CA, and the approximate independence of h_{ss}, both in qualitative agreement with the experiments.

After showing that the system sustains a dynamic steady-state with continuous turnover, we wanted to explore its response to an external perturbation. In Fig. 2G we show a steady-state cortex to which we rapidly added an additional supply of 2μM Alexa 568-actin monomers together with accessory proteins kept at their original concentration (prior to the perturbation). The figure clearly shows that the monomers are incorporated into the growing F-actin cortex at the SLB, and then advected and degraded. Following the additional supply of monomers at the SLB, the cortex thickness increases (Fig. 2H), but later returns to the steady-state behavior with a thickness that is increased by the proportion of added actin (by about ~10%). We can simulate this experiment using our 1D model, by similarly adding uniformly a small amount of actin monomers to the system which was already at steady-state. As observed in the experiments, we find that the model predicts a transient increase in the cortex thickness, before it returns to a new, slightly thicker, steady-state (Fig. 2I). This agreement further supports our advection-degradation model of the turnover and advection dynamics of the actin cortex.

In Fig. 3A,B we show that dynamics of the actin cortex growing in the presence of myosin-II motors. In the absence of CA the cortex continues to grow (Fig. 3C), similar to the system in the absence of motors (Fig. 1B,C), but with a slower rate (inset of Fig. 3C). This significant slowing down of the thickness growth in the presence of the myosin motors could arise from active forces that contract the actin network as well as the motors slowing down the residual disassembly rate. In the presence of CA the initial growth phase is later replaced by a thin cortical layer at the steady-state conditions (Fig. 3A,B, and F (inset)), similar to the behavior in the absence of motors (Fig. 1B-D).

Both with and without CA, we find that the myosin motors (Fig. 3, cyan) accumulate over time at the SLB, which is consistent with their plus-end persistent movement which directs them to the growing tips of the actin network (Fig. 3A-H, Movie S4). In the absence of CA (Fig. 3D,E) the accumulation of motors at the SLB reaches much higher values compared to the system with CA (Fig. 3G,H, Movie S4). This may be attributed to the much thicker actin layer when CA is absent, which adsorbs more motors from the solution ("antenna-effect" (42)). The continuous growth in myosin intensity at the SLB also indicates that this system does not reach a true steady-state. We note also that the myosin distribution forms an additional small accumulation which follows the second peak of the actin distribution (see arrow in Fig. 3D,E). The roughly constant density, step-like actin cortex observed in the absence of CAcan be

attributed to the contractile forces of myosin motors exerted within the network (compare to the absence of motors in Fig. 3C inset), as predicted in (40).

However, in the presence of $CA$and actin treadmilling (Fig. 3I), the myosin intensity reaches rapidly a constant steady-state value (inset of Fig. 3G), even faster than the actin distribution which exhibits a transient growth phase (Fig. 3F). In the presence of high turnover rates, the actin distribution is exponential and its functional form is not affected by the motors (in agreement with (40)). Note that both in the presence and absence of CA we find that the long-time myosin distribution has a very broad distribution that extends well beyond the visible polymerized actin layer (Fig. 3E,H). In addition, we cannot visualize the motion of individual myosin filaments, but occasionally can track the motion of large aggregates of motors which are observed to move bidirectionally in this network, some move towards the SLB and accumulate there, while others are pushed by the actin treadmilling to the edge of the cortex, where they can be released into the solution (Fig. S5 and Movies S5 and S6). We note that the steady-state shown above resides in an intermediate range of values of the concentration of the disassembly factors (Fig. 3J). Below this range the actin cortex seems to be "jammed" and no turnover is observed, while above this range the cortex thickness does not relax to a constant value and undergoes repeated bursts of growth and decay (Fig. S5 and Movie S6).

Surprisingly, the steady-state cortex with myosin motors is significantly thicker compared to the cortex without motors (Fig. 3J), which corresponds to a significant increase in the turnover speed (Fig. 3K). By taking the ratio of the turnover speed to the thickness we can estimate the disassembly rate, which we find to be independent of the presence of motors (Fig. 3K), and could be attributed to the low myosin concentration (at high concentration myosin can promote actin disassembly (43, 44). This indicates that indeed the thicker cortical layer in the presence of motors is entirely due to the increase in turnover speed. This effect of the myosin motors could arise from the motors locally pulling the network, as well as bending and deforming the actin filaments at the SLB such that there is more available space for the incorporation of new monomers. This observation is in qualitative agreement with measurements of the actin cortex in living cells, which decreases when myosin motor activity is inhibited (21).

Discussion

One outstanding observation, which is explained using a simple theoretical model (40), is the robustness of the cortical thickness to variations in the concentration of the disassembly factors. This result suggests a simple mechanism that cells can utilize to buffer concentration fluctuations and maintain a functional cortex of sufficient thickness, which is insensitive to local variations in the concentration of the disassembly machinery. We also show that transient fluctuations in the actin concentrations cause thickness variations, which quickly decay away in this dynamical system. Further studies of the cortice's robustness and response to different perturbations can now be carried out using this minimal system.

The myosin motors in our experiments get embedded into the artificial actin cortex, accumulating at the growing tips, as observed in cells in a cell-cycle dependent manner (38). The presence of myosin motors produced a cortical thickness, which we attribute to the significant myosin dependent increase in the rate of actin treadmilling speed (Fig. 3K). This feature has not been directly observed previously and suggests that future theoretical models

of this system should include stress-dependent biochemical reaction rates (45, 46), which we find to have an effect throughout the cortex thickness.

The thickness increase in the presence of myosin motors agrees with observations of cortical actin thickness in living cells (21). However, in cells the myosin activity also induced large and localized thickness fluctuations (41), which we do not observe here. The chaotic regime of repeating cycles of cortex growth and dissipation (Fig. 3J and S5) is more similar to the periodic cycles of cortex growth, condensation and detachment observed in cell extracts (47).

Conclusions

We present here a system of minimal number of purified components that exhibits long-lasting steady-state treadmilling actin cortex on a supported cell mimicking lipid bilayer (SLB). Within these artificial membrane-bound cortices, the actin turnover is polarized with polymerization confined to the membrane, depolymerization occurring away from the membrane, creating a detectable treadmilling flow that is perpendicular to the membrane. These conditions have not been previously achieved in an in-vitro system using purified components, although there may be other minimal sets that could support treadmilling conditions, due to redundancy within cells. We characterize the dynamics of this system, during its transient growth phase and final steady-state turnover regime, as function of the concentration of the disassembly factors, both in the presence and absence of myosin molecular motors.

This system enables the future systematic study of the effect of each additional component on the dynamics of the actin cortex in a manner that is impossible inside the complex environment of living cells. Our open configuration allows for the study of the actin cortex dynamics with very high spatio-temporal resolution, and highly controlled temporal manipulations of the composition, which are very difficult to achieve in living cells. This system therefore opens the door to a deeper understanding of the cellular cytoskeleton, which is fundamental for many biological processes, such as development, immunology and cancer progression. These results open the way to many possible future directions and applications, such as the study of motility in synthetic cell-like compartments, driven by the treadmilling actin cortex (13).

Materials and methods

Materials

All lipids are purchased from Avanti Polar Lipids except for labeled PIP_2 that was purchased from Echelon Biosciences. GTPγs is purchased from ROCHE. Arp2/3 complex powder was purchased from Cytoskeleton Inc.

Protein purification

G-actin is purified from rabbit skeletal muscle acetone powder by gel filtration (48), stored on ice, and used within 3-4 weeks. Actin is labeled on Cys374 with Alexa-Fluor 488 C_5 maleimide or Alexa-Fluor 568 C_5 maleimide (Invitrogen). Myosin II skeletal muscle is purified following (49) and labeled with Alexa-Fluor 568 at pairs of engineered cysteine residues (32,50).

Preparation of dynamic steady state actin cortex on supported lipid membranes

Supported lipid bilayers are formed by flowing a 1 mg mL^{-1} solution of small unilamellar vesicles (SUV) in the flow chamber. The SUVs (and SLB) lipid composition (mol %): 30% DOPE, 30% DOPC, 10% liver PI, 25% DOPS, 4.9% Brain PIP_2, 0.1% of fluorescently labeled PIP_2 (BODIPY TMR-PIP_2), supplemented with 15% cholesterol (mimicking plasma

membrane inner leaflet composition). 2μM GTPγs-activated Cdc42 is then loaded in the chamber, followed by the loading of 1μM ΔEVH1 N-WASP, where each protein is incubated for 15' at 37°C. Finally, the chamber is loaded with a solution of purified proteins that includes actin monomers (10μM), Arp2/3 complex (40nM), Profilin (2.5μM), CPs (50nM), and hCof (3μM), as well as with variable amounts of Cor1B and AIP1 (at 1:1 molar ratio) which can vary between $0-75$ nM. Myosin II motors are added in the form of small filaments, roughly consisting of 50 myosin dimers (32). The solution also includes 2mM ATP, maintained constant using an ATP-regenerating system that includes Creatin Kinase and Creatin Phosphate (32), and an anti-bleaching solution. The molar percentage of labeled actin monomers and myosin motors is 10 and 100 %, unless stated otherwise.

Microscopy techniques

Samples are imaged using a laser scanning confocal microscope (LSM 880, Zeiss Germany) in fast Airyscan mode using a ZEN software (Zeiss Germany) or with a 3i Mariana (Denver, CO) spinning disk confocal microscope, equipped with a Yokogawa W1 module and a Prime 95B sCMOS camera, and controlled by Slide Book software. Actin is excited at 488 nm and, PIP_2 or myosin motors, at 568nm.

Data quantification

The raw confocal images are preprocessed (corrected) for uneven illumination and photobleaching, and for possible image drifts problems during image acquisition. Drift correction is performed both in lateral (x, y) and axial (z) directions by using a 'registration' function from the ANTs package (51). From the processed confocal images, we first extract for each time point, the intensity of actin monomers and myosin dimers in the bulk solution, which we use as a threshold to extract the intensity (density) distributions of polymerized actin (F-actin) and myosin II motors located in the actin network (see details in SI appendix). The images are then segmented to extract the actin cortex thickness at each time point $h(t)$, which corresponds to the distance from the bottom segmentation line to the cortex outer edge (upper segmentation line). The later corresponds to the z-position where the F-actin intensity distribution drops to half its peak value. For systems in the transient growth regime, which often exhibit more than one peak, the cortex edge position refers to most distant peak. The position of the SLB (defined as $z\equiv 0$) corresponds to the membrane intensity distribution (fits to a Gaussian function) peak. From the data we also evaluate the actin disassembly rate, τ^{-1}, by measuring the decay of the fluorescence intensity of the F-actin density at the cortex's outer edge over time. The speed of actin network turnover v_{turn} is extracted from the slopes of kymograph plots generated from sequences of xz cross-section images. Similarly, the trajectories of large individual motors clusters can be extracted from kymograph plots generated from xz cross-section Maximal Intensity Projection (MIP) image sequence.
Data quantification is performed using MATLAB (MathWorks, MA, USA), Python, Huygens Professional software package (Huygens; Scientific Volume Imaging, Hilversum, Netherlands), Origin (OriginLab Corp., MA, USA), and ImageJ software.
Due to space limitation a comprehensive Method section is provided in the SI Appendix.

Acknowledgments: We thank Karsten Kruse, Itamar Kolvin, Marco Fritzsche, and Uzi Hadad for useful discussions. We thank Shira Albeck and Tamar Unger for proteins expression and

purification at the "Israel Structural Proteomics Center (ISPC)" at the Weizmann institute of science. Plasmids. We thank Dina Aranovich for protein purification and labelling. We thank Pekka Lappalainen for providing the CPs construct, Henry Higgs for the Profilin constructs, Laurent Blanchoin for the hCof construct, Bruce L. Goode for the Cor1B and AIP1 constructs, Wendell A. Lim for the ΔEVH1 N-WASP construct, and Richard A. Cerione for the Human Cdc42 construct.

Funding: Israel Science Foundation grant 2101/20 (ABG).

Author contributions:
SG Designed and performed experiments, developed all analytical methods for data quantification, analyzed the experimental results, prepared the Figures and Movies, and wrote the manuscript.
GL Developed analytical methods for data quantification.
YA Developed analytical methods for data quantification.
NP Wrote the mathematical model.
AY Wrote the mathematical model and the manuscript.
NSG Wrote the mathematical model and the manuscript.
ABG Designed and developed the experimental system, developed analytical methods for data quantification, analyzed the experimental results, and wrote the manuscript.

Competing interests

The authors declare no competing interests.

Data availability

All data is included in the manuscript and/or supporting information.

Figure captions

Fig. 1. Reconstitution of long-lasting dynamic steady state actin cortex on supported lipid bilayer. (**A**) Schematic diagram of the experimental set-up. This system includes a flow chamber coated with a supported lipid bilayer (SLB), actin nucleation factors recruited to the SLB, triggering actin network assembly and physically linking the growing actin cortex to the SLB, a pure protein solution of accessory proteins (2) that control the actin network assembly and disassembly, as well as myosin II motors. (**B**) 3D confocal images showing the spatio-temporal evolution of actin cortices (red) assembling from the SLB surface (yellow), in the presence or absence of CA, and with and without myosin motors. (**C**) Sequence of 3D confocal side-view, xz cross-section, images showing an actin cortex that continuously grow with time (left) *vs.* an actin cortex that initially grow and then evolves towards a dynamic turnover state (right). Shown are also the actin network intensity distribution profiles measured perpendicular to the SLB (white lines). (**D**) Average cortex thickness *vs.* time of the actin cortex depicted in (C, right panel) (main). Inset: same but for the actin cortex shown in (C, left panel). The mean temporal thickness $< h(t) >$ is extracted from height maps generated from segmentation of the cortex outer edge surface (SLB position corresponding to $z = 0$). Images (i-iii) of such heigh maps are provided where: (i) $t = 5\text{min}$ and (ii) $t = 11\text{min}$ are within the growth regime, and

(iii) $t = 60\text{min}$ when the system has already reached steady state. (**E**) Actin (red) and membrane (yellow) density (intensity) distribution profiles measured normal to the SLB. The actin intensity decays exponentially away from the SLB. The actin distribution peak is z-shifted with respect to the SLB position. h_{ss} is the steady state thickness measured at one half of the maximal value (see material and methods for details). Conditions: same concentrations of CA and myosin motors as in (C, right panel). (**F**) The actin cortex turnover speed v_{turn} is extracted from the slopes of Kymograph plots. New trajectories consistently emerge (white dotted lines), all displaying similar linear slopes, indicating that both the actin fluxes and the turnover velocity are long-lasting (hours) and stable over time. Same experimental conditions as in (E). (**G**) Turnover velocity against time for treadmilling actin cortices, in the presence (red dots) and absence (black dots) of myosin motors.

Fig. 2. Effect of actin disassembly rate on actin cortex turnover and steady state thickness in the absence of myosin contractility. (**A**) Turnover velocity, v_{turn}, against CA concentrations. Shown are individual data points and their corresponding $\text{mean} \pm \text{SD}$ values ($N = 40 - 50$ for each $[CA]$). The line represents fit (equation depicted in (B)) to the data ($r^2 = 0.98$). (**B**) Actin cortex disassembly rate τ^{-1} against CA concentration extracted from the decay in actin intensity measured during the transient growth phase at the cortex edge (black) or determined from the ratio of the turnover velocity and cortex thickness in the steady state regime (blue). Shown are $\text{mean} \pm \text{SD}$ values (dots). The lines represent fit to the data ($r^2 = 0.95$). (**C**) Average steady state cortex thickness, $< h_{ss} >$ against CA concentration. Shown are individual data points and their corresponding $\text{mean} \pm \text{SD}$ values ($N = 110$ for the various experimental conditions). The lines represent fit (same equation as in (B)) to the data ($r^2 = 0.96$). (**D**) Schematic description of treadmilling cortical network model (see SI model). (**E**) Spatial profiles calculated from the model at different times (solid lines), with dashed lines denoting the distribution of actin monomers. The parameters used in the calculations are given in the SI. (**F**) Asymptotic width of the total amount of polymerized actin (red dots) and turnover velocity v (blue diamonds) for different initial concentrations of soluble disassembly factor to the initial concentration of actin monomers; the width is computed at one half of the maximal value of the distribution of total polymerized actin as in the experiments. (**G-H**) **System response to an external perturbation**. (**G**) Shown is an actin cortex at dynamic steady state (green) to which we rapidly added (at $t = 23$ min) an additional supply of $2\mu\text{M}$ red actin monomers (corresponding to an addition of 20 mol %) and accessory proteins with the same original concentrations. The added actin monomers are incorporated into the growing actin cortex at the SLB (v marks the growth speed), and then advected and disassembled, as reflected in the normal density profiles of green (white) and red (red) actin. The average steady state thickness h_{ss}, prior and after disturbance: 2.54 ± 0.05 μm and 2.72 ± 0.05 μm (for both actin Alexa-Fluor 488 and 568), respectively corresponds to an increase of 10% of the steady state thickness. Bar is 5μm. Experimental conditions: $CA = 60$ nM. (**I**) Simulated width of the total polymerized actin distribution *vs.* time, after a uniform addition of 20 mol % actin monomers, which promotes an increase of $\sim 10\%$ in cortex thickness, where the initial state is the asymptotic steady-state shown in Fig. 2E ($t = 500$). The right y-axis shows the normalized width normalized to the maximal width.

Fig. 3. Actin turnover and myosin contractility govern cortex dynamics. **(A and B)** Confocal (3D (A) and side-view, xz cross-section (B), images) showing the spatio-temporal evolution of actin cortices (red) assembling from an SLB surface (not shown), in the presence

of myosin (cyan), with and without disassembly factors (CA). **(C-E)** Effect of myosin contractility on actin cortex dynamics in the *absence* of disassembly factors (CA). Shown are the actin (C) and myosin (D) density distribution profiles measured normal to the SLB at different time points. (E) Their combined density distributions at long times ($t = 100$ min). The red dashed lines in (E) mark the position (z_c) and intensity ($I(z_c)$) of the myosin density distribution peak value where the arrows in (C and E) points towards a local peak in myosin density which correlates with actin density at the cortex rear. Insets: (C) Average cortex thickness *vs.* time in the presence (blue) and absence (black) of myosin motors; (E) depicts the temporal evolution in peak position z_c and myosin intensity $I(z_c)$. The vertical black dashed lines in (C-E) mark the position of the membrane ($z = 0$). **(F-H)** Same as (C-E) but in the presence of 25nM CA. **(I)** A Kymograph plot of a treadmilling actin cortex at steady state (same myosin and CA concentrations as in (F-H)). The turnover speed v_{turn} is extracted from the slopes of Kymograph plots. **(J) Effect of [CA] and myosin contractility on the system dynamic state and average thickness at long times $t = 60$min.** Shown are individual data points and their corresponding mean $\pm$ SD values ($N = 110$ for each condition). **(K) Effect of myosin contractility on actin network turnover speed and steady state thickness.** Shown are the actin turnover speed and the steady state actin cortex disassembly rate τ^{-1}, in the absence and presence of myosin motors, at the same $[CA]$. Shown are individual data points and their corresponding mean $\pm$ SD values ($N = 40 - 50$).

References

1. Salbreux G, Charras G, Paluch E. Actin cortex mechanics and cellular morphogenesis. Trends Cell Biol. 2012;22(10):536-45.

2. Fritzsche M, Lewalle A, Duke T, Kruse K, Charras G. Analysis of turnover dynamics of the submembranous actin cortex. Mol Biol Cell. 2013;24(6):757-67.

3. Fritzsche M, Erlenkämper C, Moeendarbary E, Charras G, Kruse K. Actin kinetics shapes cortical network structure and mechanics. Science advances. 2016;2(4):e1501337.

4. Svitkina TM. Actin cell cortex: structure and molecular organization. Trends Cell Biol. 2020;30(7):556-65.

5. Blanchoin L, Boujemaa-Paterski R, Sykes C, Plastino J. Actin dynamics, architecture, and mechanics in cell motility. Physiol Rev. 2014;94(1):235-63.

6. Maître J, Turlier H, Illukkumbura R, Eismann B, Niwayama R, Nédélec F, et al. Asymmetric division of contractile domains couples cell positioning and fate specification. Nature. 2016;536(7616):344-8.

7. Munjal A, Philippe J, Munro E, Lecuit T. A self-organized biomechanical network drives shape changes during tissue morphogenesis. Nature. 2015;524(7565):351-5.

8. Bray D, White JG. Cortical flow in animal cells. Science. 1988;239(4842):883-8.

9. Bernheim-Groswasser A, Gov NS, Safran SA, Tzlil S. Living matter: mesoscopic active materials. Adv Mater. 2018;30(41):1707028.

10. Prost J, Jülicher F, Joanny J. Active gel physics. Nature physics. 2015;11(2):111-7.

11. Chugh P, Paluch EK. The actin cortex at a glance. J Cell Sci. 2018;131(14):jcs186254.

12. Liu AP, Fletcher DA. Biology under construction: in vitro reconstitution of cellular function. Nature Reviews Molecular Cell Biology. 2009;10(9):644-50.

13. Siton-Mendelson O, Bernheim-Groswasser A. Toward the reconstitution of synthetic cell motility. Cell adhesion & migration. 2016;10(5):461-74.

14. Lopes dos Santos R, Campillo C. Studying actin-induced cell shape changes using Giant Unilamellar Vesicles and reconstituted actin networks. Biochem Soc Trans. 2022;50(5):1527-39.

15. Sonal GK, Vogel SK, Mücksch J, Blumhardt P, Schwille P. Myosin-II activity generates a dynamic steady state with continuous actin turnover in a minimal actin cortex. J Cell Sci. 2018;132.

16. Carvalho K, Tsai F, Lees E, Voituriez R, Koenderink GH, Sykes C. Cell-sized liposomes reveal how actomyosin cortical tension drives shape change. Proceedings of the National Academy of Sciences. 2013;110(41):16456-61.

17. Sakamoto R, Banerjee DS, Yadav V, Chen S, Gardel ML, Sykes C, et al. Membrane tension induces F-actin reorganization and flow in a biomimetic model cortex. Communications Biology. 2023;6(1):325.

18. Wubshet NH, Wu B, Veerapaneni S, Liu AP. Differential regulation of GUV mechanics via actin network architectures. Biophys J. 2023;122(11):2068-81.

19. Clausen MP, Colin-York H, Schneider F, Eggeling C, Fritzsche M. Dissecting the actin cortex density and membrane-cortex distance in living cells by super-resolution microscopy. J Phys D. 2017;50(6):064002.

20. Chugh P, Clark AG, Smith MB, Cassani DA, Dierkes K, Ragab A, et al. Actin cortex architecture regulates cell surface tension. Nat Cell Biol. 2017;19(6):689-97.

21. Laplaud V, Levernier N, Pineau J, Roman MS, Barbier L, Sáez PJ, et al. Pinching the cortex of live cells reveals thickness instabilities caused by myosin II motors. Science Advances. 2021;7(27):eabe3640.

22. Papayannopoulos V, Prehoda KE, Snapper S, Taunton J, Lim WA. A polybasic motif allows N-WASP to act as a sensor of PIP2 density. Mol Cell. 2005;17(2):181-91.

23. Bernheim-Groswasser A, Wiesner S, Golsteyn RM, Carlier M, Sykes C. The dynamics of actin-based motility depend on surface parameters. Nature. 2002;417(6886):308-11.

24. Prehoda KE, Scott JA, Mullins RD, Lim WA. Integration of multiple signals through cooperative regulation of the N-WASP-Arp2/3 complex. Science. 2000;290(5492):801-6.

25. Noireaux V, Golsteyn RM, Friederich E, Prost J, Antony C, Louvard D, et al. Growing an actin gel on spherical surfaces. Biophys J. 2000;78(3):1643-54.

26. Xue B, Robinson RC. Guardians of the actin monomer. Eur J Cell Biol. 2013;92(10-11):316-32.

27. Koestler SA, Rottner K, Lai F, Block J, Vinzenz M, Small JV. F-and G-actin concentrations in lamellipodia of moving cells. PloS one. 2009;4(3):e4810.

28. Brieher WM, Kueh HY, Ballif BA, Mitchison TJ. Rapid actin monomer–insensitive depolymerization of Listeria actin comet tails by cofilin, coronin, and Aip1. J Cell Biol. 2006;175(2):315-24.

29. Jansen S, Collins A, Chin SM, Ydenberg CA, Gelles J, Goode BL. Single-molecule imaging of a three-component ordered actin disassembly mechanism. Nature communications. 2015;6(1):1-13.

30. Siton-Mendelson O, Bernheim-Groswasser A. Functional actin networks under construction: the cooperative action of actin nucleation and elongation factors. Trends Biochem Sci. 2017;42(6):414-30.

31. Lappalainen P, Kotila T, Jégou A, Romet-Lemonne G. Biochemical and mechanical regulation of actin dynamics. Nature Reviews Molecular Cell Biology. 2022;23(12):836-52.

32. Ideses Y, Sonn-Segev A, Roichman Y, Bernheim-Groswasser A. Myosin II does it all: assembly, remodeling, and disassembly of actin networks are governed by myosin II activity. Soft Matter. 2013;9(29):7127-37.

33. Kaminer B, Bell AL. Myosin filamentogenesis: effects of pH and ionic concentration. J Mol Biol. 1966;20(2):391-401.

34. Billington N, Wang A, Mao J, Adelstein RS, Sellers JR. Characterization of three full-length human nonmuscle myosin II paralogs. J Biol Chem. 2013;288(46):33398-410.

35. Backouche F, Haviv L, Groswasser D, Bernheim-Groswasser A. Active gels: dynamics of patterning and self-organization. Physical biology. 2006;3(4):264.

36. Ideses Y, Erukhimovitch V, Brand R, Jourdain D, Hernandez JS, Gabinet UR, et al. Spontaneous buckling of contractile poroelastic actomyosin sheets. Nature communications. 2018;9(1):1-13.

37. Sakamoto R, Murrell MP. F-actin architecture determines the conversion of chemical energy into mechanical work. Nature Communications. 2024;15(1):3444.

38. Truong Quang BA, Peters R, Cassani DA, Chugh P, Clark AG, Agnew M, et al. Extent of myosin penetration within the actin cortex regulates cell surface mechanics. Nature communications. 2021;12(1):6511.

39. Mogilner A, Edelstein-Keshet L. Regulation of actin dynamics in rapidly moving cells: a quantitative analysis. Biophys J. 2002;83(3):1237-58.

40. Joanny J, Kruse K, Prost J, Ramaswamy S. The actin cortex as an active wetting layer. The European Physical Journal E. 2013;36(5):1-6.

41. Levernier N, Kruse K. Spontaneous formation of chaotic protrusions in a polymerizing active gel layer. New Journal of Physics. 2020;22(1):013003.

42. Naoz M, Manor U, Sakaguchi H, Kachar B, Gov NS. Protein localization by actin treadmilling and molecular motors regulates stereocilia shape and treadmilling rate. Biophys J. 2008;95(12):5706-18.

43. Haviv L, Gillo D, Backouche F, Bernheim-Groswasser A. A cytoskeletal demolition worker: myosin II acts as an actin depolymerization agent. J Mol Biol. 2008;375(2):325-30.

44. Reymann A, Boujemaa-Paterski R, Martiel J, Guérin C, Cao W, Chin HF, et al. Actin network architecture can determine myosin motor activity. Science. 2012;336(6086):1310-4.

45. Bell GI. Models for the specific adhesion of cells to cells: a theoretical framework for adhesion mediated by reversible bonds between cell surface molecules. Science. 1978;200(4342):618-27.

46. Risca VI, Wang EB, Chaudhuri O, Chia JJ, Geissler PL, Fletcher DA. Actin filament curvature biases branching direction. Proceedings of the National Academy of Sciences. 2012;109(8):2913-8.

47. Krishna A, Savinov M, Ierushalmi N, Mogilner A, Keren K. Size-dependent transition from steady contraction to waves in actomyosin networks with turnover. Nature Physics. 2024;20(1):123-34.

48. Spudich JA, Watt S. The regulation of rabbit skeletal muscle contraction: I. Biochemical studies of the interaction of the tropomyosin-troponin complex with actin and the proteolytic fragments of myosin. J Biol Chem. 1971;246(15):4866-71.

49. Margossian SS, Lowey S. [7] Preparation of myosin and its subfragments from rabbit skeletal muscle. In: Methods in enzymology. Elsevier; 1982. p. 55-71.

50. Quinlan ME, Forkey JN, Goldman YE. Orientation of the myosin light chain region by single molecule total internal reflection fluorescence polarization microscopy. Biophys J. 2005;89(2):1132-42.

51. Tustison NJ, Cook PA, Holbrook AJ, Johnson HJ, Muschelli J, Devenyi GA, et al. The ANTsX ecosystem for quantitative biological and medical imaging. Scientific reports. 2021;11(1):9068.

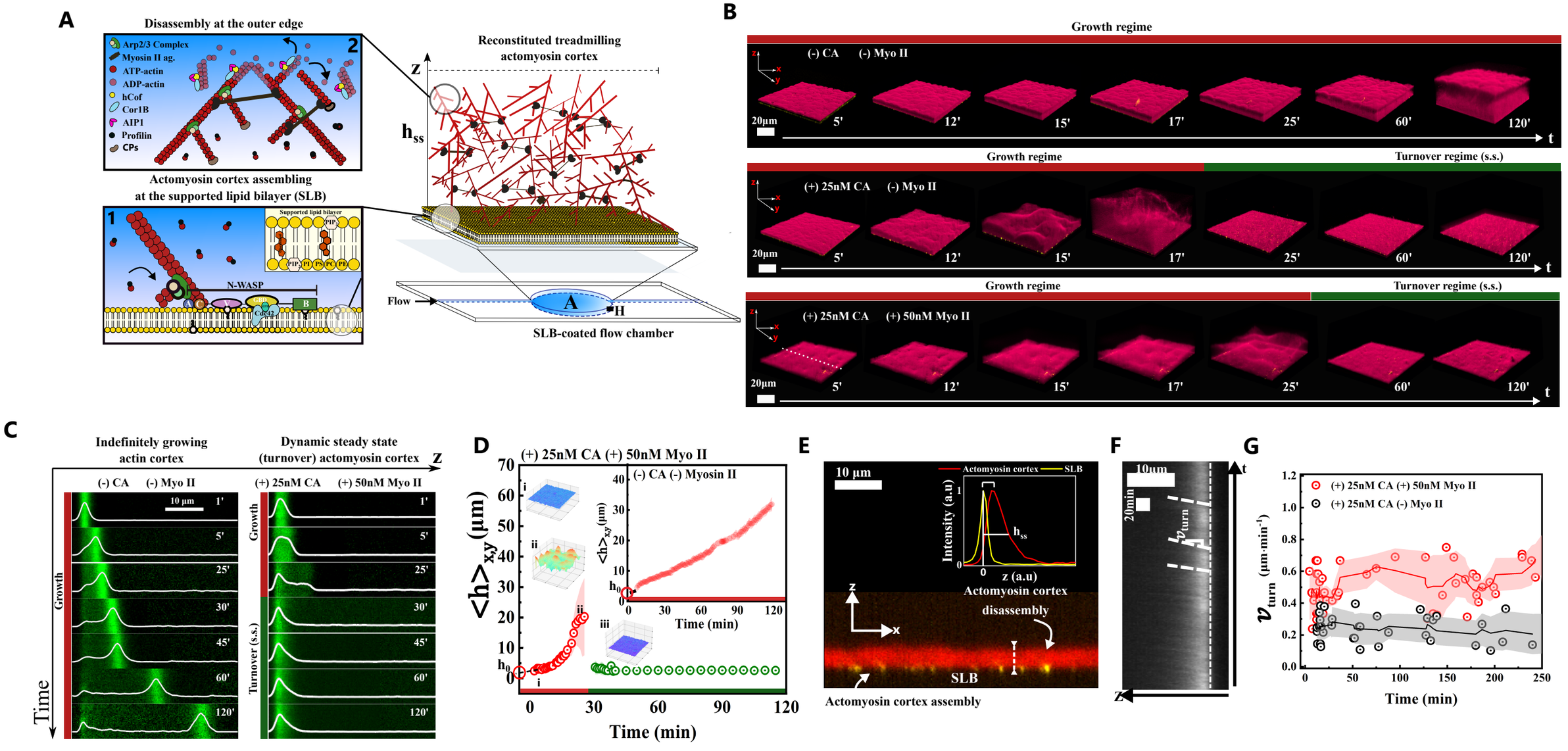
A
Disassembly at the outer edge
Arp2/3 Complex
Myosin II ag.
ATP-actin
ADP-actin
hCof
Cor1B
AIP1
Profilin
CPs
Reconstituted treadmilling actomyosin cortex
Actomyosin cortex assembling at the supported lipid bilayer (SLB)
Supported lipid bilayer
N-WASP
Flow
SLB-coated flow chamber
B
Growth regime
(-) CA (-) Myo II
(+) 25nM CA (-) Myo II
Turnover regime (s.s.)
(+) 25nM CA (+) 50nM Myo II
20µm
5'
12'
15'
17'
25'
60'
120'
C
Indefinitely growing actin cortex
Dynamic steady state (turnover) actomyosin cortex
(-) CA (-) Myo II
(+) 25nM CA (+) 50nM Myo II
10 µm
Growth
Turnover (s.s.)
Time
D
(+) 25nM CA (+) 50nM Myo II
(-) CA (-) Myosin II
Time (min)
E
10 µm
Actomyosin cortex
SLB
Intensity (a.u)
z (a.u)
Actomyosin cortex disassembly
Actomyosin cortex assembly
F
10µm
20min
G
(+) 25nM CA (+) 50nM Myo II
(+) 25nM CA (-) Myo II
Time (min)

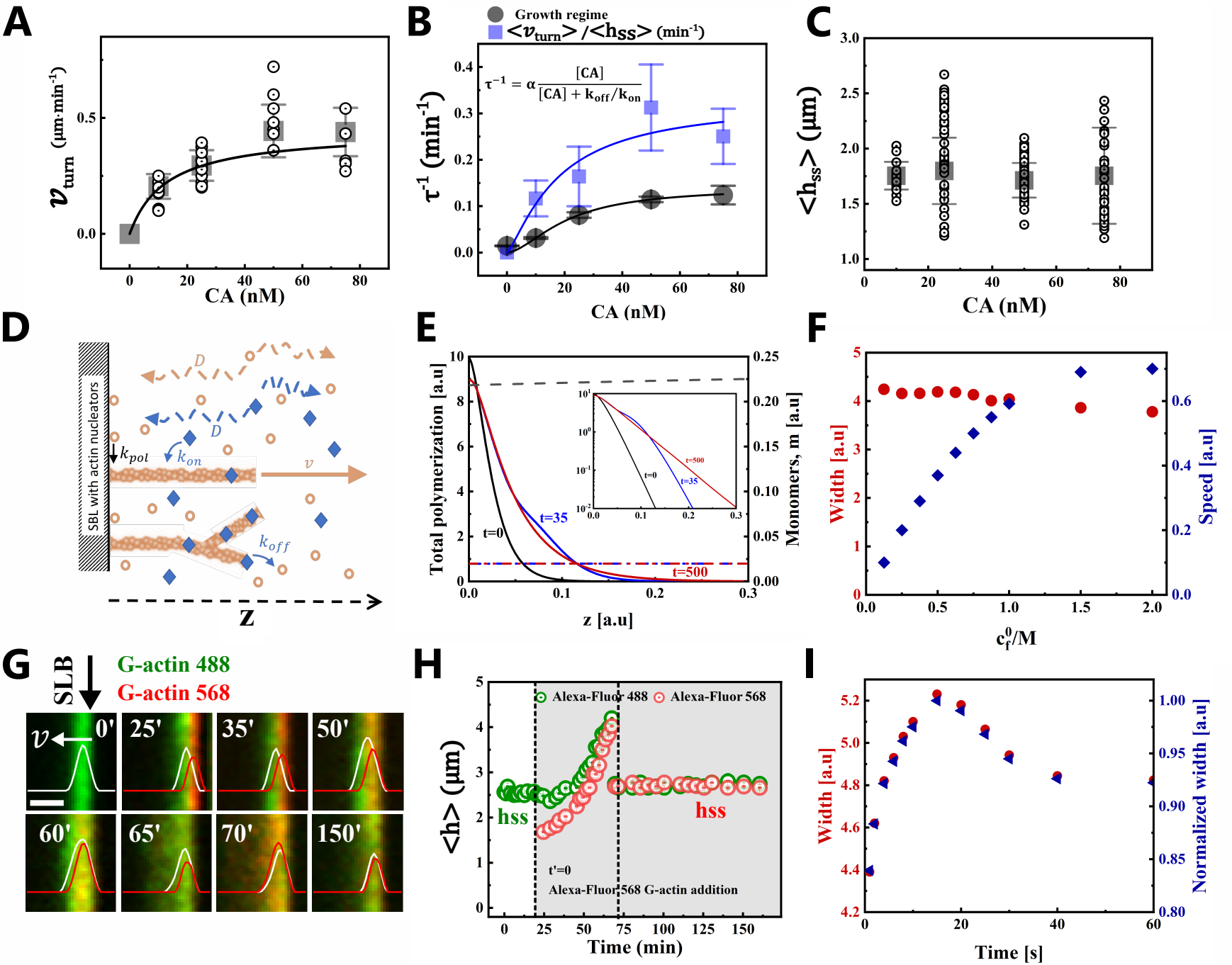
A
v_{turn} (μm·min^{-1})
CA (nM)
B
Growth regime
$\langle v_{turn}\rangle / \langle h_{ss}\rangle$ (min^{-1})
$\tau^{-1} = \alpha \frac{[CA]}{[CA] + k_{off}/k_{on}}$
τ^{-1} (min^{-1})
CA (nM)
C
$\langle h_{ss}\rangle$ (μm)
CA (nM)
D
SBL with actin nucleators
k_{pol}
k_{on}
k_{off}
D
v
Z
E
Total polymerization [a.u]
Monomers, m [a.u]
t=0
t=35
t=500
z [a.u]
F
Width [a.u]
Speed [a.u]
c_f^0/M
G
SLB
G-actin 488
G-actin 568
v
0'
25'
35'
50'
60'
65'
70'
150'
H
Alexa-Fluor 488
Alexa-Fluor 568
<h> (μm)
hss
hss
t'=0
Alexa-Fluor 568 G-actin addition
Time (min)
I
Width [a.u]
Normalized width [a.u]
Time [s]

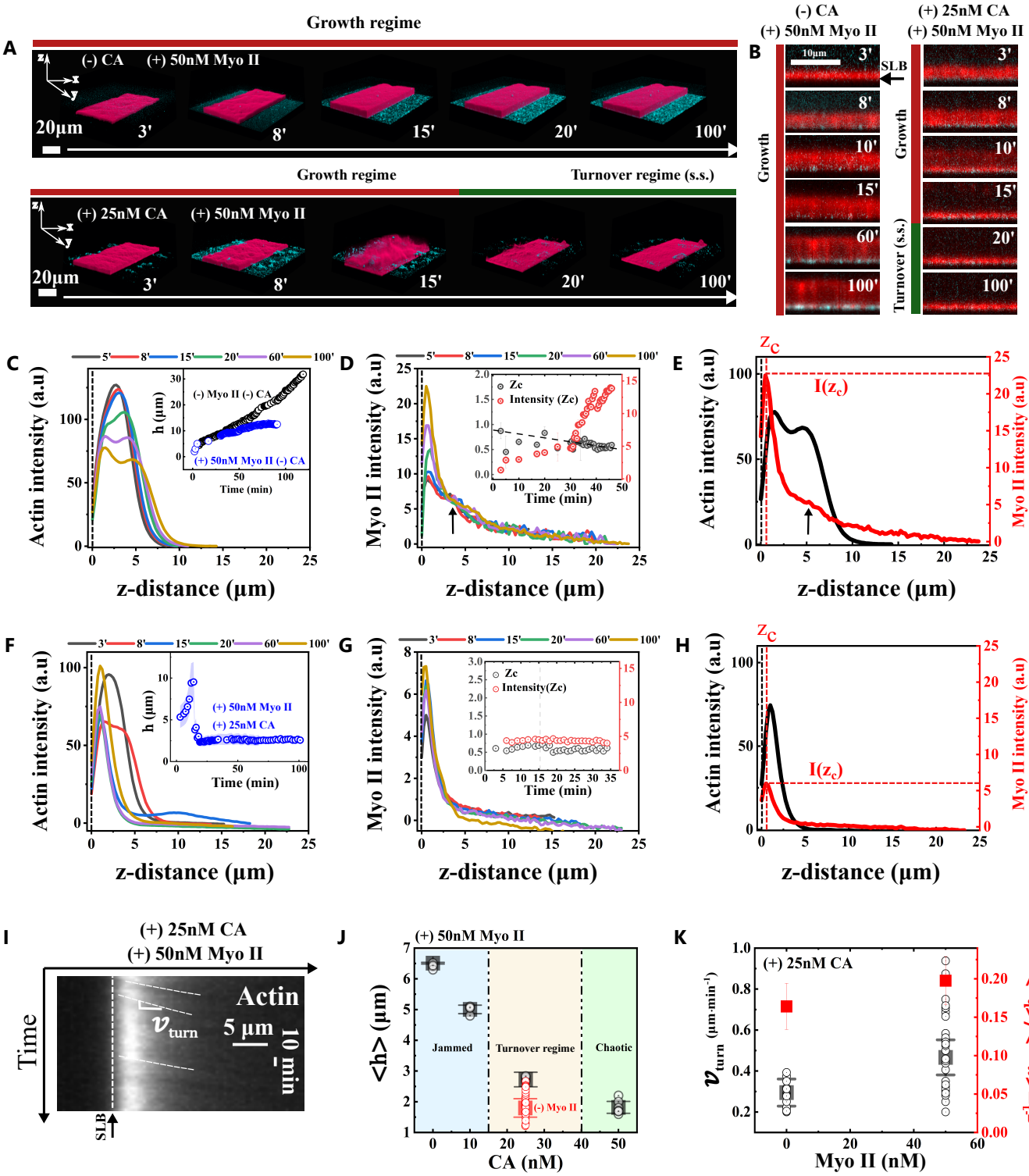
A
Growth regime
(-) CA
(+) 50nM Myo II
20µm
3'
8'
15'
20'
100'
Growth regime
Turnover regime (s.s.)
(+) 25nM CA
(+) 50nM Myo II
B
(-) CA
(+) 50nM Myo II
(+) 25nM CA
(+) 50nM Myo II
10µm
SLB
Growth
Turnover (s.s.)
C
Actin intensity (a.u)
z-distance (µm)
h (µm)
Time (min)
(-) Myo II (-) CA
(+) 50nM Myo II (-) CA
D
Myo II intensity (a.u)
Zc
Intensity (Zc)
E
Zc
I(zc)
Myo II intensity (a.u)
F
(+) 50nM Myo II
(+) 25nM CA
G
Intensity(Zc)
H
I
(+) 25nM CA
(+) 50nM Myo II
Time
Actin
5 µm
10 min
SLB
J
(+) 50nM Myo II
<h> (µm)
Jammed
Turnover regime
Chaotic
(-) Myo II
CA (nM)
K
(+) 25nM CA
Myo II (nM)